J Solid State Electrochem (2017) 21:1305–1312
DOI 10.1007/s10008-016-3485-z

ORIGINAL PAPER

A sustainable synthesis of biomass carbon sheets as excellent performance sodium ion batteries anode

Decai Qin[1,2] · **Song Chen**[1]

Received: 24 September 2016 / Revised: 27 November 2016 / Accepted: 30 November 2016 / Published online: 10 December 2016

Abstract Biomass-derived carbon (BMC) materials have attracted much attention due to their high performance and properties of abundant source. Herein, biomass carbon sheets (BMCS) from wheat straws had been successfully synthesized via a facile high temperature carbonization and expansion processes. The morphology of BMCS keeps the natural honeycomb-like shape of the cross section and the hollow tubular array structure of the vertical section with rich pores, which provides low-resistant ion channels to support fast diffusion. The (002) crystal plane reveals that the intercalation distance of carbon sheets is 0.383 nm larger than that graphite (0.335 nm), which benefits the larger sodium ion de/intercalation. By comparing different carbonization temperatures, wheat straws carbonized at 1200 °C (BMCS-1200) with well graphite microcrystallites show more excellent sodium ion storage performance than that of 900 °C (BMC-900). BMCS-1200 shows a stable reversible capacity of 221 mAh g^{-1} after 200 cycles at 0.05 A g^{-1}, while BMC-900 is 162 mAh g^{-1} after 100 cycles. And it also exhibits better rate capability (220, 109 mAh g^{-1}) than that of BMC-900 (125, 77 mAh g^{-1}) at 0.2 and 1 A g^{-1}, respectively. Finally, it delivers 89 mAh g^{-1} stable capacity after 1400 cycles at 1 A g^{-1} to prove its excellent long-term cycling stability.

Keywords Sustainable · Biomass carbon sheets · Anode · Sodium ion battery

Introduction

Grid electrical energy storage plays a significant in addressing the climate change by integrating a wide variety of renewable energy sources. Lithium ion batteries (LIBs) are currently the most promising electrical energy storage (EES) devices because of their superior power and energy density with excellent energy conversion efficiency. However, considering the large-scale applications of LIBs on grid energy storage, it would suffer an essential threat for an unbalanced lithium source distribution and high cost [1, 2]. Sodium ion batteries (SIBs), based on the Earth-abundant Na sources, represent an attractive technology for the next generation energy storage [3, 4]. However, the issue of larger size of Na ion (99 pm) compared to Li ion (59 pm) which leads to slower ion diffusion, larger volume change and structure pulverization upon charge and discharge needs to be addressed. Researchers have developed alloying metals [5, 6], metal oxides [4, 7], inorganic intercalation compound [8], and carbonaceous materials [9–11], which have been studied for SIBs, etc. as potential anode materials. However, each class of such materials, apart from carbonaceous materials, suffered a huge volume change or a high over potential due to certain intrinsic limitations of material itself, which leads to an ultra-low cyclic durability.

Recently, many explorations based on various natural biomass sources were carried out to synthesize carbon-based electrode materials for EES and environmental science owing

Electronic supplementary material The online version of this article (doi:10.1007/s10008-016-3485-z) contains supplementary material, which is available to authorized users.

✉ Song Chen
jsyccs@163.com

[1] School of Chemistry and Chemical Engineering, Yancheng Institute of Technology, Yancheng, Jiangsu 224051, China

[2] College of Materials Science and Technology, Jiangsu Key Laboratory of Materials and Technologies for Energy Conversion, Nanjing University of Aeronautics and Astronautics, Nanjing, Jiangsu 210016, China

to their low-cost, environment-friendly, and Earth abundance [12, 13]. Diverse carbonaceous materials derived from diverse biomasses such as rice straws, reed plants, and banana peels were used in LIBs or SIBs for anode [13–15] and achieved some success. But the reported biomass sources are very limited in nature and would not meet the requirements of low cost and large-scale synthesis for current EES application. As a by-product of wheat, wheat straw is an abundant biomass source in the system of wheat production. Wheat straws are annually accumulated around 529 million t/year worldwide. And Asia becomes the largest producing area with around 43% of global wheat production [16]. However, the current applications of wheat residues just are the lower added value products, such as forage, producing fuel, and others. It is worried that massive crop straw residues have influenced our environment and society due to the dispose mode of burning. Hence, motivating the "trash to treasure" is an urgently growing pressure. Wheat straws are transformed into high-value products, which would effectively optimize our environment and sources in Fig. 1. Furthermore, wheat straws could become a better choice to apply for EES for their wider distribution, easier to collect, and lower cost than other biomass sources.

Herein, naturally abundant wheat straw as biomass carbon (BMC) source was used to fabricate biomass carbon sheets (BMCS) for SIBs by a simple high temperature carbonization and expansion procedure. Specifically, wheat straws were firstly carbonized in an inert atmosphere at the temperature of 900 °C (namely BMC-900) and 1200 °C (BMCS-1200), respectively, which was followed by an expansion process. It is believed that this tailored carbonization and expansion process will help to enlarge the space of carbon sheets meanwhile to enhance the specific surface area, which finally facilitates the diffusion and de/intercalation of sodium ion in the carbon materials. When used as anode for SIBs, both carbon materials derived from wheat straws show excellent sodium ion storage performance. The results indicate that wheat straws that carbonized specimen at higher temperature (BMCS-1200) could deliver a higher stable reversible capacity and exhibit a better rate capability than that of BMC-900. Besides, AGCS shows a superior long-term cycling stability, which is indispensable to the future SIBs application. Generally speaking, wheat straws can support a low-cost, abundant, and sustainable carbon source to allow the large scale synthesis of carbon materials with attractive sodium ion storage performance.

Fig. 1 Illustration of wheat straws for the different utilization

Experimental

Materials preparation

The naturally dried wheat straws as raw materials were used to synthesize BMC. They were manually separated into stalks and leaf. The stalks were cleaned with deionized water and ethanol. Then, the materials were thoroughly dried in 110 °C for 24 h, and 2 g samples were carbonized at 900 °C (BMC-900) and 1200 °C (BMCS-1200) in a tubular furnace for 2 h at a heating rate of 2 °C min^{-1} under nitrogen flow (100 sccm), respectively. After the carbonization, the gained products were immersed in 0.1 M HCl at 40 °C for 4 h to remove impurities and rinsed with massive distilled water until it was neutral. The above products were immersed in a mixture solution containing H_2SO_4 (98 %) and H_2O_2 (30 %) (volume ratio 3:1) at 35 °C for 2 h under stirring. Then, some deionized water was added and stirred for an additional 4 h. Finally, H_2O_2 (30 %) solution was dropwise added to the mixture until no gas bubbles evolved, and the products were washed and dried.

Material characterization

Thermogravimetry (TG) was performed on a thermogravimetric analyzer (NETZSCH STA 409PC) in a N_2 flow rate of 20 ml min^{-1} with a heating rate of 10 °C min^{-1}. The field emission scanning electron micrograph (FESEM, LEO 1530 VP, Germany), the transmission electron microscope (TEM, Jem-2100F), and the high-resolution transmission electron microscope (HR-TEM, JEOL-2010F, Japan) measurements are used to characterize the materials morphology and microstructure. The X-ray diffraction (XRD, Bruker D8 Advance power X-ray diffractometer, Germany) analyses were conducted at 40 kV with CuKα radiation (λ = 0.15418 nm) at a scanning rate of 0.050° s^{-1} in a 2θ = 10–90°. Laser confocal microzone Raman spectroscopy (HORIBA LabRAM HR Evolution, Japan) was utilized to analyze the bonding characteristics and the existence of defects using a 488 nm laser beam. The Brunauer–Emmett–Teller (BET) surface area was tested by nitrogen adsorption/desorption isotherms at 77.521 K (ASAP 2020 analyzer, USA). Electrical conductivity of carbon products was measured by ST-2722

semiconductor resistivity of the powder tester at 10 Mpa (Suzhou Jinge Electroic Co., Ltd).

Electrochemical measurements

Typically, the anode electrode was prepared by mixing 80 % wt active material, 10 % wt acetylene black, and 10 % wt polyvinylidene fluoride (PVDF) in *N*-methyl-2-pyrrolidone (NMP) via the slurry coating technique. First, the slurries were uniformly coated onto thin copper foil current collectors and then dried under the vacuum condition at 110 °C for 12 h. Finally, the coin cells (CR2032) were assembled in an argon-filled glove box via utilizing sodium metal foil as the counter, glass microfiber filters as separator, and 1 M $NaClO_4$ solution mixture of ethylene carbonate (EC) and diethyl carbonate (DEC) (volume ratio = 1:1) as electrolyte, where the oxygen and moisture contents were sustained below 0.1 ppm. All electrochemical measurements were performed on coin cells at room temperature. All the cyclic voltammetry (CV) measurements were tested on a CHI 770D workstation at a sweeping rate of 0.1 mV s^{-1} from 0.01 to 3.0 V. The CT2001A of Land Battery Measurement System Instrument (LAND Electronic Co.) was used to measure galvanostatically discharged/charged at different current densities between 0.01 and 3 V (vs Na/Na^+). Electrochemical impedance spectroscopy (EIS) measurements were conducted on the same workstation with an AC amplitude of 5 mV from 1 MHz to 0.01 Hz frequency scope.

Results and discussion

The morphologies of wheat straws before and after carbonization were firstly characterized by SEM. Figure 2a, b shows wheat straw natural morphologies of the cross section and vertical section, respectively. The figure shows an analogous honeycomb cross section and a hollow tubular array vertical section with linked macropores (marked with circles). The SEM images of BMCS-1200 and BMC-900 (Fig. 2e, f) keep similar morphologies regardless of carbonization temperature and still retain the natural pore structure of wheat straws. Although the morphologies are similar, the tubular wall turns thinner with an elevated carbonization temperature. These characteristics support fast diffusion of electrolyte and

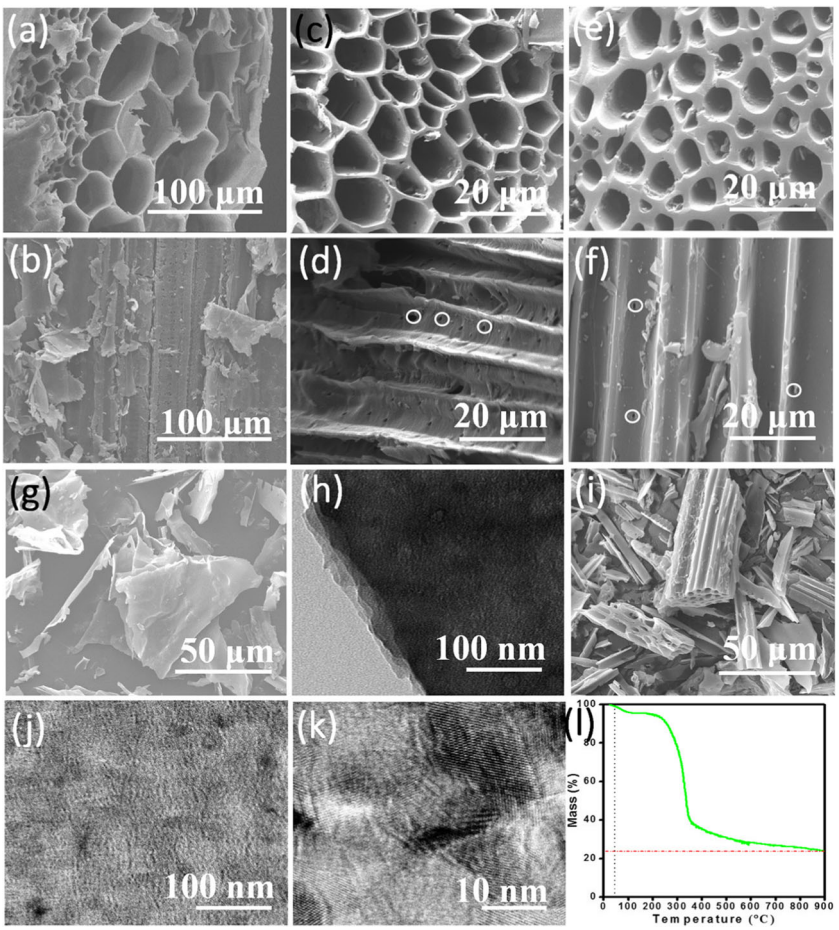

Fig. 2 SEM images of **a** cross section and **b** vertical section of natural wheat straws; **c** cross section and **d** vertical section of BMCS-1200; **e** cross section and **f** vertical section of BMC-900; **g** carbon sheets of BMCS-1200; **h** TEM image of BMCS-1200; **i** SEM image of BMC-900; **j**, **k** high-resolution TEM (HRTEM) images of BMCS-1200; and **l** TG profile of wheat straws during the carbonization process

available accommodation for volume expansion during sodium ion de/intercalation and provide more electrochemical active sites. Besides, BMCS-1200 displays a lamellar structure in Fig. 2g with more loose analogous graphitic sheets demonstrated by Fig. 2h. By contrast, BMC-900 just shows the bulk of the particulates in Fig. 2i. To further explain the microstructure of carbon sheets, the high-resolution TEM (HRTEM) images of Fig. 2j, k were conducted. Figure 2j shows more pores in AGCS-1200, and Fig. 2k reveals well graphite microcrystallites to supply effective electrons transmission and the excellent rate capability for SIBs [17, 18]. To analyze the thermal decomposition process of wheat stalk in nitrogen atmosphere, thermal gravimetric analysis (TGA) was performed in Fig. 2l. Biomass is usually composed of cellulose, lignin, and hemicellulose. The carbonization process mainly ascribes to the pyrolysis of these polymers. Here, TGA curve exhibits an obvious mass loss region from 230 to 800 °C. It is well known that cellulose usually decomposes from the temperature of 200 to 400 °C along with the decomposition of hemicellulose and lignin decomposes at a broad temperature range of 150–750 °C. During the carbonization process, the micropore, mesopore, and macropore would be developed for the gas evaporation and the pyrolysis of polymers, resulting in total the volume and the BET surface area variation [19].

Nitrogen adsorption/desorption isotherm measurements were used to investigate the porosity features of BMCS-1200 and BMC-900. In Fig. 3a, both two carbon samples all display typical type I/IV isotherms with a hysteresis loop, implying the existence of micropore, mesopore, and macropore. Specifically, the type I isotherms show a significant upward trend in $P/P_0 < 0.45$, indicating abundant micropores. The presentation of obvious hysteresis loops in $P/P_0 = 0.45–0.95$ suggests the existence of massive mesopores. And the adsorption process ascends very steeply due to the capillary condensation in mesopores. Besides, all isotherms exhibit an obvious uptrend at the highest relative pressure of $P/P_0 > 0.95$, suggesting the existence of macropores. In addition, based on the IUPAC descriptions, a hysteresis loop should be classified as four types [20]. It is evident that hysteresis loops of Fig. 3a are in agreement with type H4 loop features owing to adsorption/desorption in plate-like materials with narrow slit-like pores [21]. The pore size distribution (PSD) profile of Fig. 3b is mainly about 3.8 nm of diameter pore in BMCS-1200 and BMC-900. Besides, the PSD profile peak of BMCS-1200 is lower than BMC-900, which delivers a smaller specific surface area of 111.58 $m^2\ g^{-1}$ and total pore volume of 0.0878 $cm^3\ g^{-1}$ for BMCS-1200 (1295.21 $m^2\ g^{-1}$ and 0.7684 $cm^3\ g^{-1}$ correspond to BMC-900). The significantly reduced specific surface area from BMC-900 to AGCS-1200 is ascribed to the improvement of the degree of graphite microcrystallites, which will be demonstrated from XRD results.

Figure 3c shows the X-ray diffraction (XRD) patterns of BMCS-1200 and BMC-900 specimens. They all display two obvious diffraction peaks. The broad peak of BMCS-1200 at $2\theta = 22.87°$ is triggered by reflections of parallel-laminated graphene layers (PLGLs) from the (002) crystal planes, while the peak at $2\theta = 43.02°$ attributes to the (101) crystal planes of

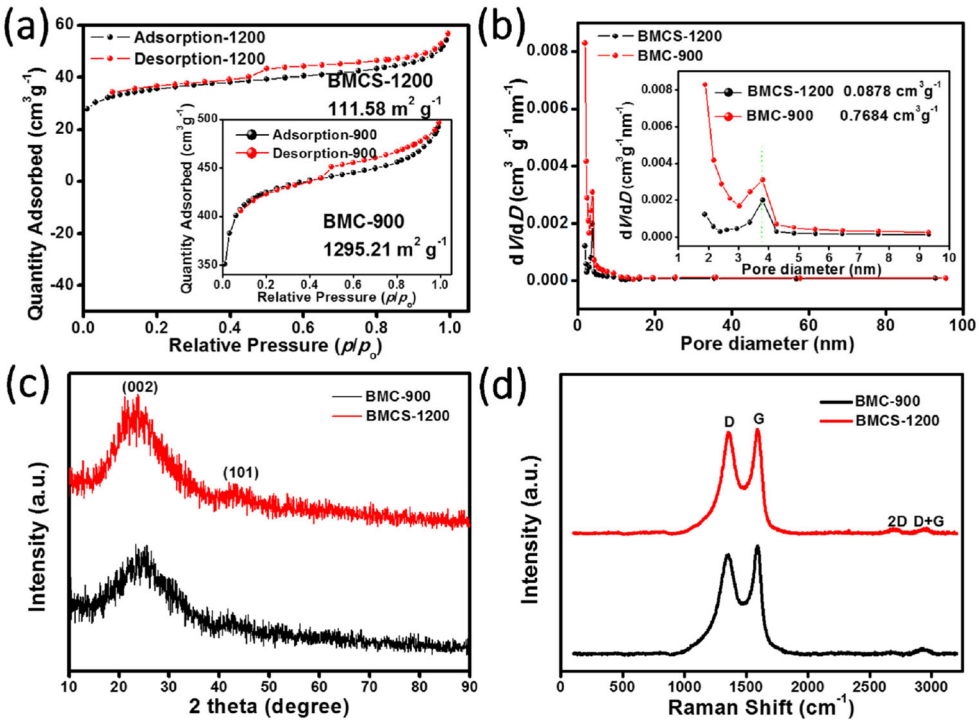

Fig. 3 **a** Nitrogen adsorption/desorption isotherms of BMC-900 (the *inset*) and BMCS-1200, **b** pore diameter distribution of BMC-900 and BMCS-1200 (the *inset* is partial detail), and **c** XRD patterns of BMCS-1200 and BMC-900 specimens. **d** Raman spectra of BMCS-1200 and BMC-900

sp^2-C [22]. Here, the (002) and (101) crystal planes peaks of BMC-900 are at 2θ = 24.07° and 42.46°, respectively. The intensity of (002) peak of BMCS-1200 is higher than that of BMC-900, which reveals that the *c*-axis length (L_c) of the graphitic domains increase. And the higher intensity of the (101) peak in BMCS-1200 suggests an increase of the degree of graphitization. The interlayer distance of graphite sheets of BMCS-1200 from the peak (002) is calculated to be 0.383 nm by the Bragg equation (0.367 nm for BMC-900), which is larger than that of graphite *d*-spacing (0.335 nm). It will greatly be helpful to benefit the de/intercalation for the larger sodium ions. The average thickness L_c (*c*-axis length) of the pseudographitic domain is computed by the Scherrer equation. The average thickness of BMCS-1200 is 1.03, implying 2–3 PLGLs. Yet, the average thickness of BMC-900 is 0.67. The thickness tends to higher value with the higher carbonization temperature, implying much more graphitic domains to be formed in BMCS-1200. High crystallized graphite benefits to produce massive PLGLs. Smith et al. [23] evaluated the proportion of PLGLs with empirical *R*-factor value (ESI, an illustration for the definition of the ratio *R* in Fig. S1), and the high value shows plenty of PLGLs. Here, the *R*-factors of BMCS-1200 and BMC-900 are 2.63 and 2.34 by adopting the (002) crystal planes of the XRD peaks, which reveal the formation of PLGLs easily at higher temperature. Numerous PLGLs of BMCS-1200 are supposed to display better electrochemistry performance, which could be confirmed by the following electrochemical characterization. Figure 3d shows the Raman spectra of BMCS-1200 and BMC-900, which shows the obvious broad disordered D-bands at ≈1360 cm^{-1} and in-plane bond-stretching motion G-bands at ≈1588 cm^{-1}. And the D-bands attribute to the disorder-induced sp^3-C atoms from the aromatic rings, yet G-bands ascribe to the in-plane vibration of sp^2-C atoms [24]. The values of D- and G-bands are utilized to evaluate the order degree of graphite. An increase of the D-band intensity predicates an ascent in the number of the defects [25]. To the spectrum of BMCS-1200, the intensity of D-band is nearly the same as that G-band, suggesting much more edge defects and the phase of the structural distortion due to the higher carbonization temperature. The I_D/I_G ratio is about 0.98 for BMCS-1200, while BMC-900 is about 0.91. The higher I_D/I_G ratios are identified significantly that amorphous states shift to much more graphitic structures with numerous defects [26]. Interestingly, BMCS-1200 shows second index 2 D and D + G peaks, which are also in accordance with their graphitic structure with more defects [27]. This result agrees well with the XRD and HRTEM results. The I_{2D}/I_G ratio could be used as an indicator to associate the electrical conductivity performance with their structures. As a result, an electrical conductivity of BMCS-1200 is 153.8 S cm^{-1}, which is about fourth higher than that BMC-900 (41.6 S cm^{-1}). The excellent electrical conductivity and graphitic structure with more defects of wheat stalk-derived carbon materials will greatly be in favor of the high performance of SIBs anode.

In order to investigate the electrochemical performance of BMC-900 and BMCS-1200, cyclic voltammetry (CV) curves and galvanostatic charge/discharge cycling were conducted. Figure 4a, b displays the initial three CV curves of BMC-900 and BMCS-1200, respectively, in the potential range of

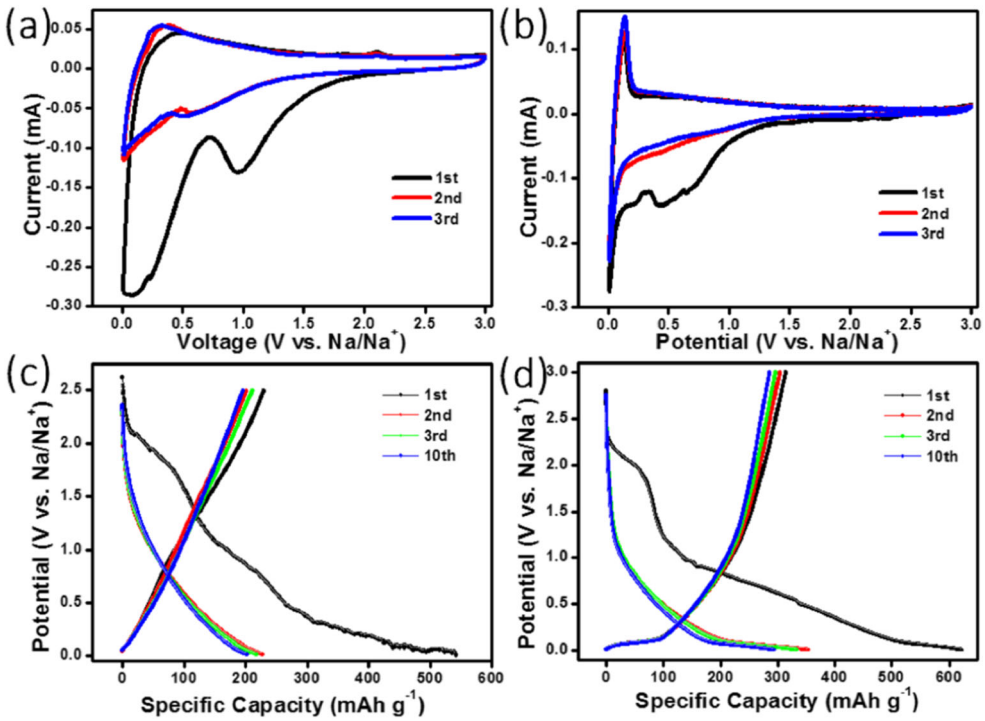

Fig. 4 Initial three cyclic voltammetry curves of **a** BMC-900 and **b** BMCS-1200 at a scan rate of 0.1 mV s^{-1}; galvanostatic charge/discharge cycling of **c** BMC-900 and **d** BMCS-1200 at a current density of 0.05 A g^{-1}

0.01–3 V at a scan rate of 0.1 mV s^{-1}. It is obvious that the first scan is distinct from the subsequent ones in both of them. BMC-900 shows a narrow reduction peak about 1.0 V in the first scan, yet the wide reduction region between 0.22 and 1.0 V is for BMCS-1200. And the phenomena disappear in the subsequent 2 cycles. These peaks might correspond to the formation of solid electrolyte interface (SEI) and the decomposition of the electrolyte [28]. The CV curves of BMCS-1200 have extremely sharp cathodic and less sharp anodic peaks between 0.01 and 0.22 V. The cathodic peaks are ascribed to insertion of sodium ion into the microvoids [29], while the anodic peaks correspond to their extraction [11]. However, the anodic peaks occurred a hysteresis, which ascribes to the graphitic structure with more defects [30]. The extraction of sodium ion occurs in less sharp anodic peaks than extremely sharp cathodic peaks, revealing much more sodium ion extraction [11]. By contrast, BMC-900 shows a broad cathodic peaks and anodic peaks than that BMCS-1200. The subsequent two CV curves of both of them show good repeatability, which delivers the good stability and reversible performance during sodium ion insertion/extraction. Meanwhile, the rectangular shapes of the CV curves of BMCS-1200 at different scan rate suggest weak capacitive-like behavior for sodium ion storage (ESI, Fig. S2). Figure 4c, d shows the half-cell galvanostatic charge/discharge cycling of the first, second, third, and tenth cycles for BMC-900 and BMCS-1200 at a current density of 0.05 A g^{-1}. At the first discharge/charge cycle, BMC-900 delivers charge/discharge capacities of 230.2/542.9 mAh g^{-1} with an initial coulombic efficiency (CE) of 42.4 %, yet 315.1/623.6 mAh g^{-1} for BMCS-1200 with an initial CE of 50.53 %, respectively. Notably, the CE of both them rises rapidly over 95 % after the tenth cycle. BMC-900 and BMCS-1200 still maintain high discharge capacities of about 204 and 293 mAh g^{-1} after tenth cycle, respectively. In addition, a broad slope below about 1.0 V appears in both BMC-900 and BMCS-1200. The profiles of sloping and the plateau regions correspond to the pairs of broad and sharp peaks in CV curves, respectively. Besides, the large initial irreversible capacity attributes to the formation of SEI layer, the electrolyte decomposition, as well as the irreversible trapping of sodium ions at PLGLs [17, 31], which agrees well with the CV results.

To evaluate the cycling capacity retention performance, the cycling life measurements of BMC-900 and BMCS-1200 at a current density of 0.05 and 0.2 A g^{-1} are conducted and the results are shown in Fig. 5a, b, respectively. The excellent long-term cyclability of both of them is crucial for future application in the EES. BMCS-1200 in Fig. 5a shows much higher cycling discharge capacity retention of about 224 mAh g^{-1} after 100 cycles than that BMC-900 of 160 mAh g^{-1} at a current density of 0.05 A g^{-1}. In addition, BMCS-1200 still exhibits well cycling discharge capacity retention of circa 221 mAh g^{-1} after 200 cycles. When increasing the current density from 0.05 to 0.2 A g^{-1}, similar results could be confirmed. After the initial 5 cycles activation process at a current density of 0.05 A g^{-1}, BMCS-1200 in Fig. 5b shows a higher discharge capacity of about 150 mAh g^{-1} than that circa 135 mAh g^{-1} of BMC-900 after 200 cycles at a high current density of 0.2 A g^{-1}. So far, only few reports have exhibited such a high capacity values over 200 cycles at a similar current density [13, 32, 33]. Figure 5c shows the rate performances of BMC-900 and BMCS-1200 at different current densities from 0.05 to 2 A g^{-1}. The initial discharge capacities of BMCS-1200 are circa 255, 220, 151, and 109 mAh g^{-1} at a current density of 0.1, 0.2, 0.5, and 1 A g^{-1}, respectively. Moreover, a higher reversible capacity of circa 80 mAh g^{-1} can be delivered at a super high current density of 2 A g^{-1}. To the best of our knowledge, only few researches on biomass carbon as SIBs anode have exhibited a higher capacity value over 80 mAh g^{-1} at a similar current density [9, 32–37]. BMC-900 displays an initial discharge capacity of about 144, 125, 90, and 77 mAh g^{-1} at the corresponding current density, respectively. Furthermore, a higher reversible capacity of about 60 mAh g^{-1} at a high current density of 2 A g^{-1} is still higher than that of some reported results [32, 35]. More importantly, when the current densities are transformed back into the initial discharge condition of 0.05 A g^{-1}, BMCS-1200 and BMC-900 still deliver reversible capacities of about 240 and 150 mAh g^{-1}, respectively. By comparing to BMC-900, BMCS-1200 shows a higher capacity value and better rate capability due to highly graphitic structure with numerous defect sites. Here, another reason is observed from the electrochemical impedance spectroscopy (EIS) before the electrochemical tests, which can also explain the excellent electrochemical performance for BMCS-1200 in Fig. 5d. The Nyquist plots of both of them display a semicircle in the high frequency section owing to the resistance of charge transfer between SEI and electrolyte interface and a sloping straight line in the low frequency section due to the Warburg impedance for the sodium ion diffusion in solid states of the electrode materials (ESI, the equivalent circuit in Fig. S3). The charge transfer resistance of BMCS-1200 is 70 Ω, yet 425 Ω of BMC-900 is seven times than that BMCS-1200 (ESI, more detailed information in Table S1), where it reveals the good charge transport capability and electrolyte infiltration to support the excellent performance for BMCS-1200.

Although BMCS-1200 delivers some good properties at a low current density, long-term cycle capability under a greater current density also needs to evaluate its performance and meet future high power application. As shown in Fig. 5e, BMCS-1200 reveals a high capacity of around 160 mAh g^{-1} in the sixth cycle at a super high current density of 1 A g^{-1} after an activation over initial 5 cycles at a current density of 0.05 A g^{-1}. After 100 circles, it shows a reversible capacity of about 100 mAh g^{-1}. Moreover, the capacity attenuation is very much small in the rest of 1300 cycles, namely a fading

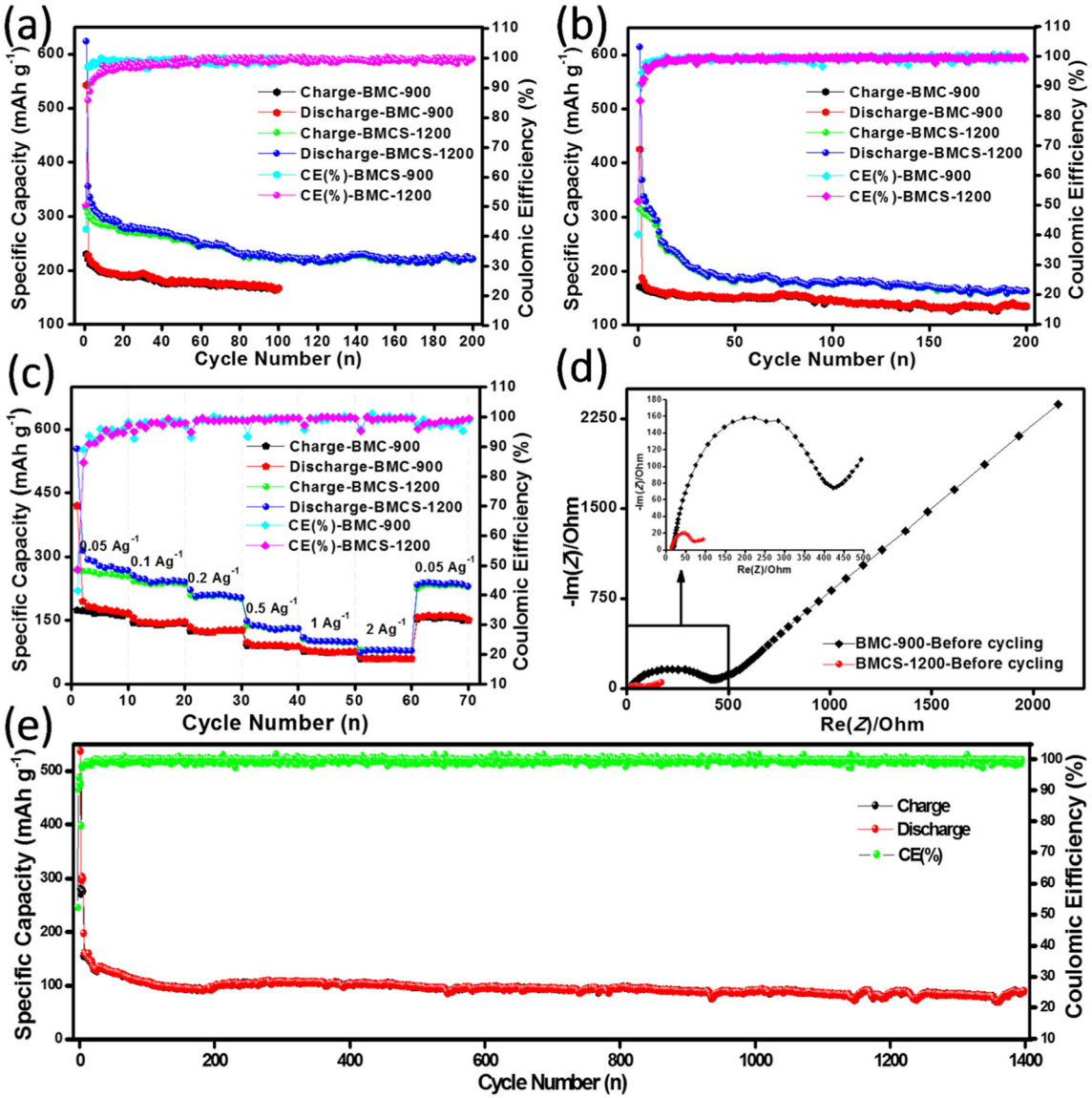

Fig. 5 Comparison for cycling capacity retention of **a** BMC-900 and BMCS-1200 at a current density of 0.05 A g^{-1} and **b** BMC-900 and BMCS-1200 at a current density of 0.2 A g^{-1}. **c** Comparison for rate performance of BMC-900 and BMCS-1200 at different current densities. **d** Electrochemical impedance spectra of BMC-900 and BMCS-1200 before electrochemical test. **e** Long-term cycling performance for BMCS-1200 at a super high current density of 1 A g^{-1}

of 11 mAh g^{-1}. Finally, it delivers an around 89 mAh g^{-1} stable capacity over 1400 cycles.

Conclusion

In our study, we successfully demonstrated that wheat stalks could serve as an ideal biomass carbon source to tailor SIBs anode with attractive electrochemical performance. Based on the environmentally-friendly and naturally-abundant wheat straws, BMCS-1200 was fabricated by the tailored high temperature carbonization and subsequent expansion process. The synthesis methods could not only enlarge the interlayer spacing of graphite domain in them, which allowed the sodium ion de/intercalation to improve battery performances, but also generate abundant pores, which facilitated the diffusion of electrolyte and transportation of sodium ion. As a result, BMCS-1200 has highly crystallized graphite domains with numerous defect sites to support an outstanding sodium ion storage performance. In brief, BMCS-1200 expresses a good electrochemical performance to support the low-cost, environmentally-friendly and sustainable sodium ion battery anode.

Acknowledgements The present work was financially supported by the Yancheng City Cooperative Innovation Fund Project (No.

YKA201219), the Natural Science Foundation of Jiangsu Province, China (No. BK20141261), and the joint research project among industry and university as well as institute of Jiangsu Province, China (No. BY2015057-35).

References

1. Vikström H, Davidsson S, Höök M (2013) Lithium availability and future production outlooks. Appl Energy 110:252–266
2. Kim SW, Seo DH, Ma X, Ceder G, Kang K (2012) Electrode materials for rechargeable sodium-ion batteries: potential alternatives to current lithium-ion batteries. Adv Energy Mater 2:710–721
3. Palomares V, Serras P, Villaluenga I, Hueso KB, Carretero-González J, Rojo T (2012) Na-ion batteries, recent advances and present challenges to become low cost energy storage systems. Energy Environ Sci 5:5884–5901
4. Slater MD, Kim D, Lee E, Johnson CS (2013) Sodium-ion batteries. Adv Fun Mater 23:947–958
5. Xie X, Kretschmer K, Zhang J, Sun B, Su D, Wang G (2015) Sn@CNT nanopillars grown perpendicularly on carbon paper: a novel free-standing anode for sodium ion batteries. Nano Energy 13:208–217
6. Dai KH, Zhao H, Wang ZH, Song XY, Vince B, Liu G (2014) Toward high specific capacity and high cycling stability of pure tin nanoparticles with conductive polymer binder for sodium ion batteries. J Power Sources 263:276–279
7. Srirama H, Kuppan S, Vishwanathan R, Palani B (2013) A rationally designed dual role anode material for lithium-ion and sodium-ion batteries: case study of eco-friendly Fe3O4. PCCP 15:2945–2953
8. David L, Bhandavat R, Singh G (2014) MoS2/graphene composite paper for sodium-ion battery electrodes. ACS Nano 8:1759–1770
9. Wang H, Yu W, Shi J, Mao N, Chen S, Liu W (2016) Biomass derived hierarchical porous carbons as high-performance anodes for sodium-ion batteries. Electrochim Acta 188:103–110
10. Luo XF, Yang CH, Peng YY, NW P, Ger MD, Hsieh CT, Chang JK (2015) Graphene nanosheets, carbon nanotubes, graphite, and activated carbon as anode materials for sodium-ion batteries. J Mater Chem A 3:10320–10326
11. Zhu JD, Chen C, Lu Y, Ge YQ, Jiang H, Fu K, Zhang XW (2015) Nitrogen-doped carbon nanofibers derived from polyacrylonitrile for use as anode material in sodium-ion batteries. Carbon 94:189–195
12. Chen P, Wang LK, Wang G, Gao MR, Ge J, Yuan WJ, Shen Y, Xie A, SH Y (2014) Nitrogen-doped nanoporous carbon nanosheets derived from plant biomass: an efficient catalyst for oxygen reduction reaction. Energy Environ Sci 7:4095–4103
13. GY X, Han JP, Ding B, Nie P, Pan J, Dou H, Li HS, Zhang XG (2015) Biomass-derived porous carbon materials with sulfur and nitrogen dual-doping for energy storage. Green Chem 17:1668–1674
14. Jun L, Peter K, Aken PA, Van JM, Yan Y (2015) Energy storage materials from nature through nanotechnology: a sustainable route from reed plants to a silicon anode for lithium-ion batteries. Angew Chem 54:9632–9636
15. Lotfabad EM, Ding J, Cui K, Kohandehghan A, Kalisvaart WP, Hazelton M, Mitlin D (2014) High-density sodium and lithium ion battery anodes from banana peels. ACS Nano 8:7115–7129
16. Kim S, Dale BE (2004) Global potential bioethanol production from wasted crops and crop residues. Biomass Bioenergy 26: 361–375
17. Wang HG, Wu Z, Meng FL, Ma DL, Huang XL, Wang LM, Zhang XB (2013) Nitrogen-doped porous carbon nanosheets as low-cost, high-performance anode material for sodium-ion batteries. ChemSusChem 6:56–60
18. Yang T, Qian T, Wang MF, Liu J, Zhou JQ, Sun ZZ, Chen MZ, Yan CL (2015) A new approach towards the synthesis of nitrogen-doped graphene/MnO2 hybrids for ultralong cycle-life lithium ion batteries. J Mater Chem A 3:6291–6296
19. Li W, Yang K, Peng J, Zhang L, Guo S, Xia H (2008) Effects of carbonization temperatures on characteristics of porosity in coconut shell chars and activated carbons derived from carbonized coconut shell chars. Ind Crop Prod 28:190–198
20. Sing KSW (1985) Reporting physisorption data for gas/solid systems with special reference to the determination of surface area and porosity. Pure Appl Chem 57:603–619
21. Kruk M, Jaroniec M (2001) Gas adsorption characterization of ordered organic-inorganic nanocomposite materials. Chem Mater 13: 3169–3183
22. Fey TK, Lee DC, Lin YY, Kumar TP (2003) High-capacity disordered carbons derived from peanut shells as lithium-intercalating anode materials. Synth Met 139:71–80
23. Smith AJ, MacDonald MJ, Ellis LD, Obrovac MN, Dahn JR (2012) A small angle X-ray scattering and electrochemical study of the decomposition of wood during pyrolysis. Carbon 50:3717–3723
24. Marta S, Fuertes AB (2014) Direct synthesis of highly porous interconnected carbon nanosheets and their application as high-performance supercapacitors. ACS Nano 8:5069–5078
25. Shao YY, Zhang S, Engelhard MH, Li GS, Shao GC, Wang Y, Liu J, Aksay IA, Lin YH (2010) Nitrogen-doped graphene and its electrochemical applications. J Mater Chem 20:7491–7496
26. Paredes JI, Villar-Rodil S, Solís-Fernández P, Martínez-Alonso A, Tascón JMD (2009) Atomic force and scanning tunneling microscopy imaging of graphene nanosheets derived from graphite oxide. Langmuir ACS J Surf Colloids 25:5957–5968
27. CY S, YP X, Zhang WJ, Zhao JW, Tang XH, Tsai CH, Li LJ (2009) Electrical and spectroscopic characterizations of ultra-large reduced graphene oxide monolayers. Chem Mater 21:5674–5680
28. Bommier C, Luo W, Gao W-Y, Greaney A, Ma S, Ji X (2014) Predicting capacity of hard carbon anodes in sodium-ion batteries using porosity measurements. Carbon 76:165–174
29. Cao YL, Xiao LF, Sushko ML, Wang W, Schwenzer B, Xiao J, Nie ZM, Saraf LV, Yang ZG, Liu J (2012) Sodium ion insertion in hollow carbon nanowires for battery applications. Nano Lett 12: 3783–3787
30. Kaskhedikar NA, Maier J (2009) Lithium storage in carbon nanostructures. Adv Mater 21:2664–2680
31. Wang LP, Yu L, Wang X, Srinivasan M, ZJ X (2015) Recent developments of electrode materials for sodium ion batteries. J Mater Chem A 3:9353–9378
32. Prabakar SJR, Jeong J, Pyo M (2015) Nanoporous hard carbon anodes for improved electrochemical performance in sodium ion batteries. Electrochim Acta 161:23–31
33. Li DD, Zhang L, Chen HB, Ding LX, Wang SQ, Wang HH (2015) Nitrogen-doped bamboo-like carbon nanotubes: promising anode materials for sodium-ion batteries. Chem Commun 51:16045–16048
34. Luo XF, Yang CH, Peng YY, Pu NW, Ger MD, Hsieh CT, Chang JK (2015) Graphene nanosheets, carbon nanotubes, graphite, and activated carbon as anode materials for sodium-ion batteries. J Mate Chem A 3:10320–10326
35. Saravanan KR, Mullaivananathan V, Kalaiselvi N (2015) Dual hetero atom containing bio-carbon: multifunctional electrode material for high performance sodium-ion batteries and oxygen reduction reaction. Electrochim Acta 176:670–678
36. LM W, Buchholz D, Vaalma C, Giffin GA, Passerini S (2016) Apple-biowaste-derived hard carbon as a powerful anode material for Na-ion batteries. Chemelectrochem 3:292–298
37. Fonseca WS, Meng XH, Deng D (2015) Trash to treasure: transforming waste polystyrene cups into negative electrode materials for sodium ion batteries. ACS Sustain Chem Eng 3:2153–2159